Green and Facile Fabrication of Hollow Porous MnO/C Microspheres from Microalgaes for Lithium-Ion Batteries

Yang Xia,[†] Zhen Xiao,[‡,§] Xiao Dou,[†] Hui Huang,[†] Xianghong Lu,[†] Rongjun Yan,[†] Yongping Gan,[†] Wenjun Zhu,[†] Jiangping Tu,[‡] Wenkui Zhang,[†,*] and Xinyong Tao[†,*]

[†]College of Chemical Engineering and Materials Science, Zhejiang University of Technology, Hangzhou 310014, People's Republic of China, [‡]Department of Materials Science and Engineering, Zhejiang University, Hangzhou 310027, People's Republic of China, and [§]College of Materials Science and Engineering, China Jiliang University, Hangzhou 310018, People's Republic of China

ABSTRACT Hollow porous micro/nanostructures with high surface area and shell permeability have attracted tremendous attention. Particularly, the synthesis and structural tailoring of diverse hollow porous materials is regarded as a crucial step toward the realization of high-performance electrode materials, which has several advantages including a large contact area with electrolyte, a superior structural stability, and a short transport path for Li^+ ions. Meanwhile, owing to the inexpensive, abundant, environmentally benign, and renewable biological resources provided by nature, great efforts have been devoted to understand and practice the biotemplating technology, which has been considered as an effective strategy to achieve morphology-controllable materials with structural specialty, complexity, and related unique properties. Herein, we are inspired by the natural microalgae with its special features (easy availability, biological activity, and carbon sources) to develop a green and facile biotemplating method to fabricate monodisperse MnO/C microspheres for lithium-ion batteries. Due to the unique hollow porous structure in which MnO nanoparticles were tightly embedded into a porous carbon matrix and form a penetrative shell, MnO/C microspheres exhibited high reversible specific capacity of 700 mAh g^{-1} at 0.1 A g^{-1}, excellent cycling stability with 94% capacity retention, and enhanced rate performance of 230 mAh g^{-1} at 3 A g^{-1}. This green, sustainable, and economical strategy will extend the scope of biotemplating synthesis for exploring other functional materials in various structure-dependent applications such as catalysis, gas sensing, and energy storage.

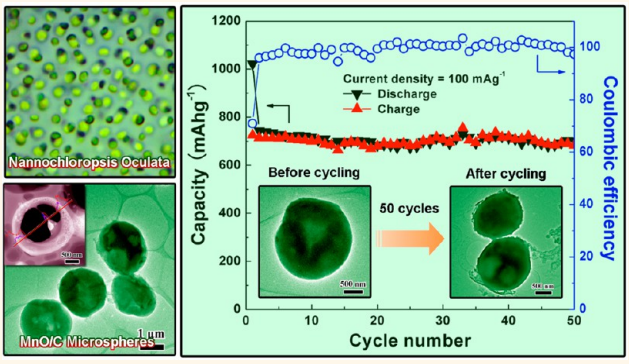

KEYWORDS: microalgae · biotemplate · MnO/C · hollow · porous structure · lithium-ion batteries

With the rapid development of portable electronic devices and hybrid electric vehicles, rechargeable lithium-ion batteries with high storage capacity and cycling stability are considered to be the versatile, clean, and promising power source. However, owing to the relatively low capacity of 370 mAh g^{-1}, high sensitivity to electrolyte, and poor cycling stability and rate capability, the commercial anode material of graphitic carbon could not meet the high power and energy density requirements of next-generation lithium-ion batteries. Unlike conventional graphite materials, transition metal oxides, as first reported by Tarascon and co-workers,[1,2] are based on an unusual conversion reaction mechanism and display extremely high reversible capacities.

Among various transition metal oxides, manganese oxides (MnO,[3−20] MnO_2,[21−26] Mn_2O_3,[27,28] and Mn_3O_4[29−31]) have attracted considerable interests because of their excellent electrochemical properties. In particular, MnO has a high theoretical capacity (756 mAh g^{-1}), a low operation potential (1.032 V *vs* Li/Li^+), as well as its natural abundance and environmental benignity, which is a promising anode material for lithium-ion batteries.[11−14] Nevertheless, the use of pure MnO is still hampered by low rate capability arising from kinetic limitations and rapid capacity fading resulting from severe agglomeration and drastic volume change during the charge/discharge

* Address correspondence to msechem@zjut.edu.cn, tao@zjut.edu.cn.

Received for review May 12, 2013 and accepted July 28, 2013.

Published online July 29, 2013
10.1021/nn4023894

process.[3−10] To date, tremendous efforts have been made to tackle the above problem. An effective strategy is synthesizing nanosized particles to shorten the diffusion length for electrons and lithium ions.[5,8,9] The second approach is constructing nanocomposites with a carbonaceous matrix, which acts as both a volume buffer and a conductive network to absorb the internal stress and increase the electrical conductivity.[3,4,7−9,13] The third strategy is fabricating hollow or porous micro/nanostructures in the electrode materials. These hollow or porous micro/nanostructures with cavity and void space can enhance the capacity retention by reversibly accommodating large volume changes.[32,33] Therefore, if nanosized MnO particles could be assembled or embedded into a conductive matrix and form a hollow porous micro/nanostructure, it will be one of the most effective approaches toward high-performance MnO electrode materials.

There is no doubt that nature is the greatest teacher in the world. It has already provided us one-, two-, and three-dimensional elaborate architectures with multiple sizes ranging from nanoscale to macroscale.[34] More importantly, these biological resources are inexpensive, abundant, and renewable. Therefore, scientists and engineers are inspired by nature to develop biotemplating techniques. So far, many classical examples have been well-established in oxides,[35−41] carbides,[42−48] metals,[49−53] chalcogenides,[54−56] even ternary metal oxides,[57−59] and phosphates[60−63] with various biotemplates. Particularly, our recent research demonstrated that the rational utilization of biotemplating strategy can realize high performance of energy storage/conversion electrode materials.[39,42,62]

In the present study, we attempt to design and fabricate a novel MnO/C composite with hollow porous microstructures *via* a facile biotemplating technique. Compared to other artificial/biological templates, the natural biological material of microalgae named *Nannochloropsis oculata* (a sphere-shaped microalgae with an average diameter of 2 μm, abbreviated as *N. oculata*; see Supporting Information Figure S1a) used in this work has three distinguishing features: (i) Easy availability. *N. oculata* cells have a fast growth rate. They can double their biomass in less than 1 day. Additionally, they are easy to cultivate and harvest. According to the recent literature, a realistic value of microalgae biomass production lies between 15 and 25 ton/ha/year.[64] (ii) Biological activity. The cell wall of *N. oculata* is mainly composed of polysaccharides. So *N. oculata* cells could adsorb and take up metal ions *via* electrostatic interactions, which are different from artificial templates.[35,65] (iii) Carbon source. *N. oculata* cells are able to accumulate large quantity of lipid inside their cells, and they contain lots of carbohydrates.[64] As a result, they could serve as a natural carbon source for fabricating a hollow porous carbon matrix (Figure S1b−d). Hence, we believe that the synthesis of novel MnO/C electrode materials derived from *N. oculata* cells will be a good example to achieve the perfect combination of nature and technology.

RESULTS AND DISCUSSION

The main process of preparing hollow porous MnO/C microspheres is illustrated in Figure 1. First, *N. oculata* cells were concentrated and purged of unwanted materials before using. Subsequently, *N. oculata* cell solution was added into the $KMnO_4/Na_2SO_4$ precursor solution. After the immersion process, *N. oculata*/MnO_2 composites could be easily synthesized *via* the biosorption and spontaneous redox deposition of metal ions on the *N. oculata* surface. In order to ensure that MnO nanoparticles could be strongly anchored into composite microspheres, the polystyrene (PS) film was coated on precursors. During the heat treatment, the carbonaceous organic compounds arising from *N. oculata* and PS could both decompose to carbon, as well as form a reducing atmosphere to transform MnO_2 to MnO. Finally, these MnO nanocrystals will be successfully embedded into porous carbonaceous matrices and constituted hollow MnO/C microspheres.

The typical X-ray powder diffraction (XRD) patterns of the *N. oculata*/MnO_2 precursor and MnO/C composites are presented in Figure 2a. There are two obvious diffraction peaks in the precursor. According to the previous report,[25] this pattern can be assigned to MnO_2 phase (JCPDS No. 42-1169). In this work, the weak peak signals of *N. oculata*/MnO_2 precursors can be attributed to the following two reasons. On the one hand, *N. oculata*/MnO_2 precursors contain lots of amorphous carbonaceous organic compounds. Thus the background of the XRD pattern in the low degree ($2\theta < 30°$) is very high, which will cover some diffraction peaks of MnO_2. On the other hand, *N. oculata*/MnO_2 precursors are in a poorly crystalline state since the redox reaction occurs at room temperature without further heat treatment. From the scanning electron microscopy (SEM) images (Figure 2b,c), it clearly depicts that *N. oculata*/MnO_2 precursors are well-dispersed microspheres with diameters ranging from 1.5 to 2 μm, which perfectly replicate the morphology and size of *N. oculata* cells. After an annealing process in a flowing nitrogen atmosphere at 500 °C for 4 h, all the diffraction peaks can be indexed to cubic MnO with an *Fm*3*m* (225) space group (JCPDS No.07-0230) as shown Figure 2a. No other impurities can be found. These results demonstrate that the *N. oculata*/MnO_2 precursor coated with PS could transform successfully to MnO/C composites, and the biotemplate of *N. oculata* has no effect on the crystal structure of MnO. Interestingly, there is no obvious morphology and size change in MnO/C composites (Figure 2d,e). The spherical structure can still be well kept. After a careful comparison, the hollow

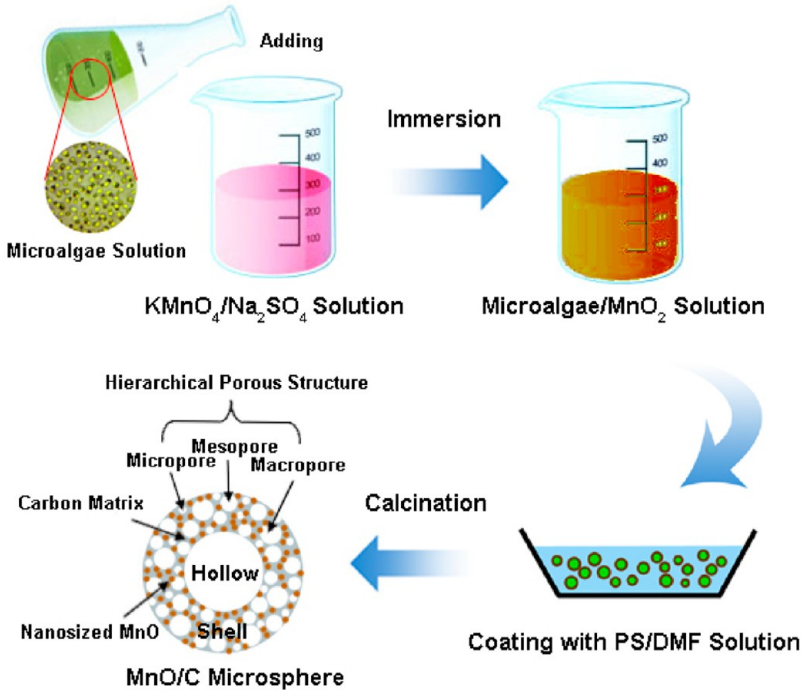

Figure 1. Schematic illustration of the fabrication process of hollow porous MnO/C microspheres.

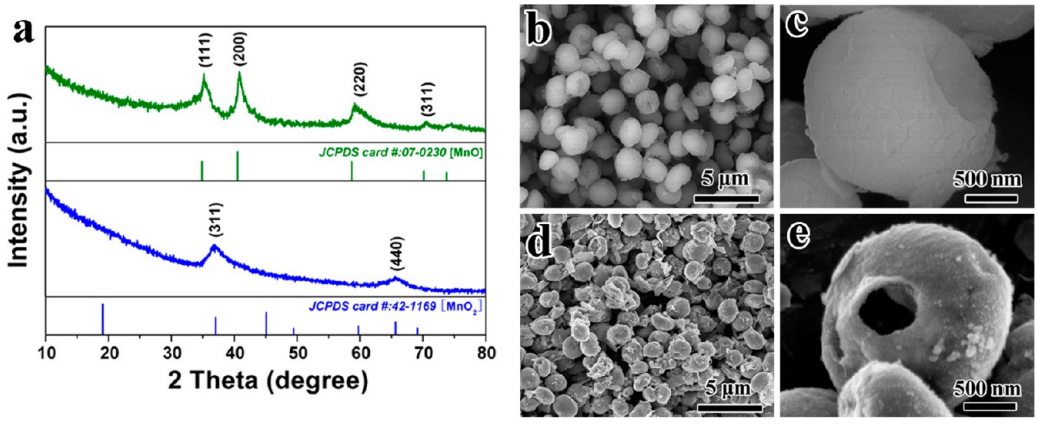

Figure 2. (a) XRD patterns of the as-prepared samples (the top is MnO/C sample; the bottom is N. oculata/MnO_2 precursor). (b, c) SEM images of N. oculata/MnO_2 precursor. (d,e) SEM images of MnO/C microspheres.

interior feature of MnO/C microspheres can be also observed, which could be attributed to the pyrolysis of the tender core of *N. oculata* during the heat treatment.

X-ray photoelectron spectroscopy (XPS) measurements were conducted to confirm the oxidation states of Mn in *N. oculata*/MnO_2 precursors and MnO/C composite. As shown in the Mn 2p spectrum of *N. oculata*/MnO_2 precursors (Figure 3), the binding energies of Mn 2p3/2 and Mn 2p1/2 are 642.1 and 653.9 eV, respectively, indicating 4+ oxidation state for Mn.[26] Meanwhile, the binding energies of Mn 2p3/2 and Mn 2p1/2 in MnO/C are 641.3 and 653.3 eV, which are in good agreement with those reported for MnO.[11] Additionally, the quantitative XPS analyses also indicate that the atomic ratio of Mn to O is approximately 0.5 in *N. oculata*/MnO_2 precursors and 1 in MnO/C composite, which are in good accordance with the results of XRD (Figure 2a).

Transmission electron microscopy (TEM) examination exhibits the detailed microstructure of the MnO/C sample. As shown in Figure 4a,b, MnO/C microspheres have a uniform spherical morphology with a particle size similar to that of SEM results (Figure 2d,e). A highly porous framework is observed on the shell of MnO/C microspheres (Figure 4c). The high-resolution TEM (HRTEM) image taken from the outside edge of the MnO/C sample (Figure 4d) clearly demonstrates that this unique porous structure is composed of MnO nanocrystals anchored into the amorphous carbon matrix with the distinct fringe spacings of about 0.226 nm, corresponding to (200) planes of cubic

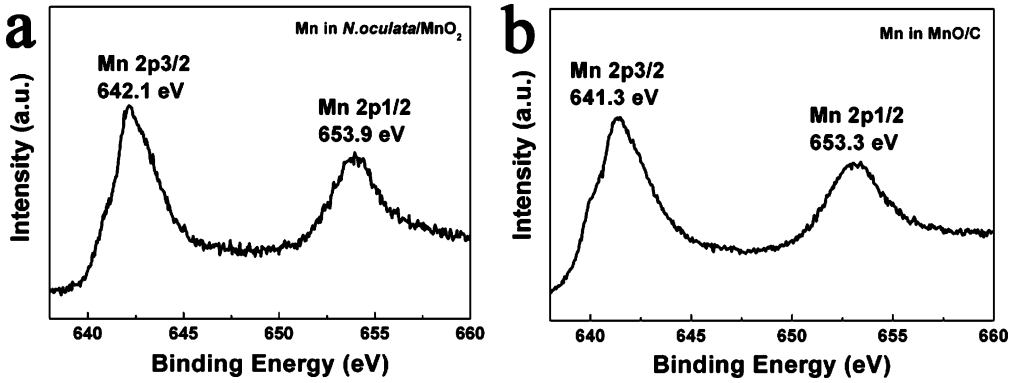

Figure 3. Mn 2p XPS spectra of N. oculata/MnO_2 precursors (a) and MnO/C composite (b).

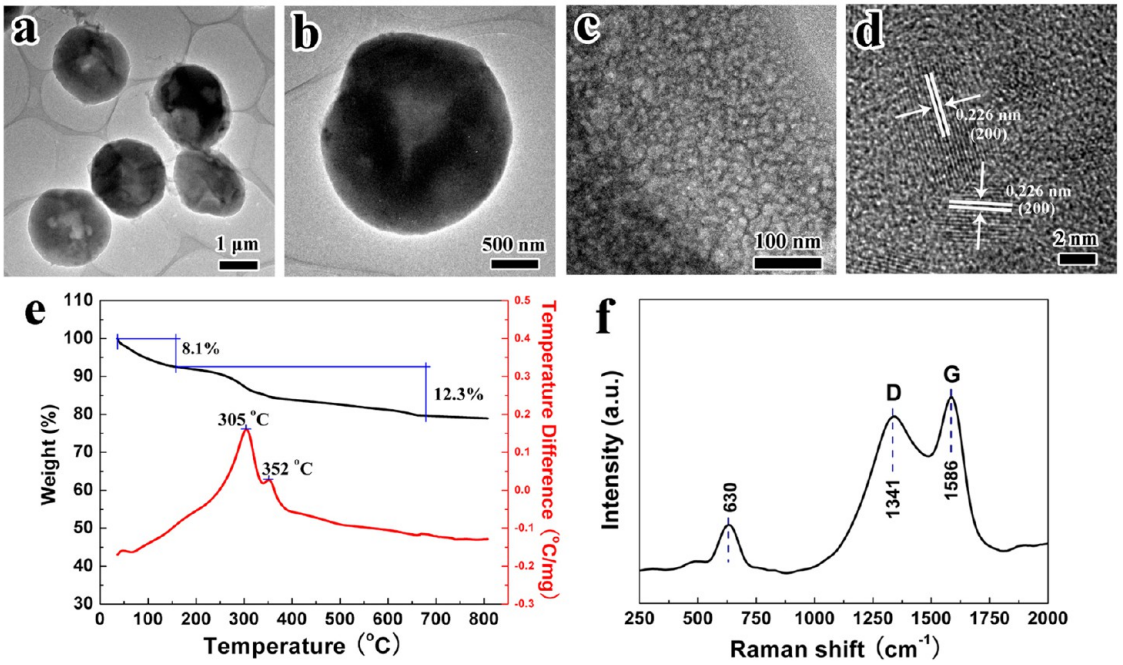

Figure 4. (a,b) TEM images of MnO/C microspheres. (c) High-magnification TEM image taken from the edge of an individual MnO/C microsphere. (d) Typical HRTEM image of MnO/C microspheres. (e) TGA-DSC curves of MnO/C microspheres. (f) Raman spectrum of MnO/C microspheres.

MnO. Moreover, in order to clarify the roles of PS, the sample without coating PS was studied, as well. As seen in Figure S2, abundant MnO_2 nanocrystals are attached to each other on the surface of the sample without PS coating. Besides, there is no obvious carbon layer on the surface, which is quite different from the sample with PS coating. So it can be easily concluded that PS coating layers, on the one hand, ensured the phase transformation from MnO_2 to MnO. On the other hand, PS coating layers also guarantee that MnO nanoparticles could entirely embed into the carbon matrix. From the above comparison, the MnO/C sample obviously will achieve better structural integrity than the sample without PS coating.

In order to evaluate the actual carbon content and its quality, thermal analysis and Raman spectroscopy were both performed. The thermal decomposition characteristic of MnO/C microspheres was investigated by thermogravimetric analysis and differential scanning calorimetry (TGA-DSC) under oxygen atmosphere (Figure 4e). A weight loss of 8.1% (W_1) up to 150 °C is due to the dissipation of absorbed water. Subsequently, there is a distinct weight loss (W_2) of 12.3% from 120 to 700 °C, which can be attributed to the integrative effect of the weight loss (arising from the combustion of carbon to CO_2) and the weight gain (arising from the oxidation of MnO). Meanwhile, two obvious endothermic peaks can be found at 305 and 352 °C. Zaki *et al.* reported that MnO will transform to Mn_2O_3 after a heat treatment between 500 and 1050 °C in oxygen atmosphere.[66] This oxygenation process of MnO to Mn_2O_3 will cause about 11.28% weight gain. Therefore, the actual amount of carbon can be calculated from the 12.3% weight loss (W_2) plus the 11.28% weight gain of the oxidation of MnO. Consequently, the carbon content of MnO/C

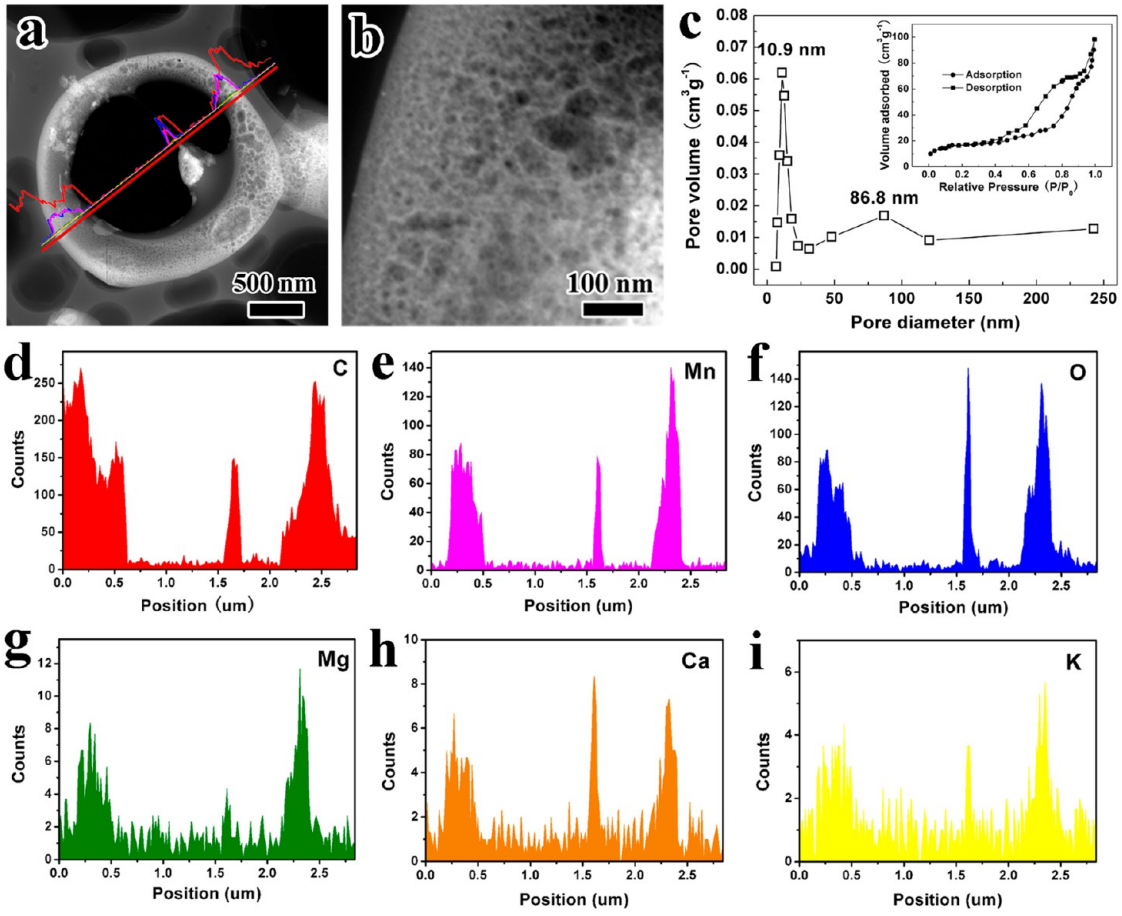

Figure 5. (a) Cross section STEM image of MnO/C microspheres. (b) High-magnification STEM image of the surface of MnO/C microspheres. (c) Pore size distribution curve calculated from the adsorption branch by the BJH model. The inset is the nitrogen adsorption−desorption isotherm loop. (d−i) Corresponding results of line-scan STEM-EDS analysis.

microspheres is about 23.6%. In the Raman spectrum (Figure 4f), a small peak observed at 630 cm^{-1} belongs to Mn_3O_4 rather than MnO. Mai *et al.* found that MnO will easily transforms to Mn_3O_4 because of the local heating effect and photochemically induced transformations under beam irradiation.[20] Two obvious peaks around 1341 and 1586 cm^{-1} are related to the A_{1g} vibration mode of the disordered carbon (D-bond) and the E_{2g} vibration mode of the ordered graphitic carbon (G-bond), respectively.[9] A small I_D/I_G intensity ratio of 0.94 indicates a high ordering degree of carbon in the sample, which is favorable to enhance the electrical conductivity and keep the structural integrity of MnO/C during charge−discharge processes.[3,39,62]

To further verify the porous hollow structure and the composition of MnO/C microspheres, cross section scanning transmission electron microscopy (STEM) images and line-scan elemental mapping are supplied. Figure 5a vividly presents the hollow nature of MnO/C mircospheres. Combined with the intensity profiles of elementals along the red straight line, each element signal (Figure 5d−i) exhibits the similar tendency, which is coincident with the STEM image and further indicates the hollow structure in the MnO/C microsphere. Additionally, the detailed elemental compositions were examined using energy-dispersive spectroscopy (EDS) (Figure S3). The main elements are C, Mn, and O. Trace elements of Mg, Ca, and K can also be detected; however, the contents are extremely low, which can almost be ignored. Hereby, these trace elements from *N. oculata* only have no effect on the composition of the MnO/C sample. Moreover, the porous texture of the MnO/C sample with a wide pore size distribution in the range of 10−100 nm can be identified clearly in Figure 5b. Such highly porous structure could be derived from the decomposition of carbonaceous organics (lipid in core and polysaccharides in cell wall) in *N. oculata* cells and PS coating layers during the carbonization process. The Brunauer−Emmett−Teller (BET) specific surface area and porosity were studied by nitrogen adsorption−desorption analysis (Figure 5c). The BET specific surface area of *N. oculata*-templated MnO/C microspheres is measured to be about 76.9 $m^2\ g^{-1}$, which is higher than that of previously reported MnO-based electrodes (Table S1). The Barrett−Joyner−Halenda (BJH) pore

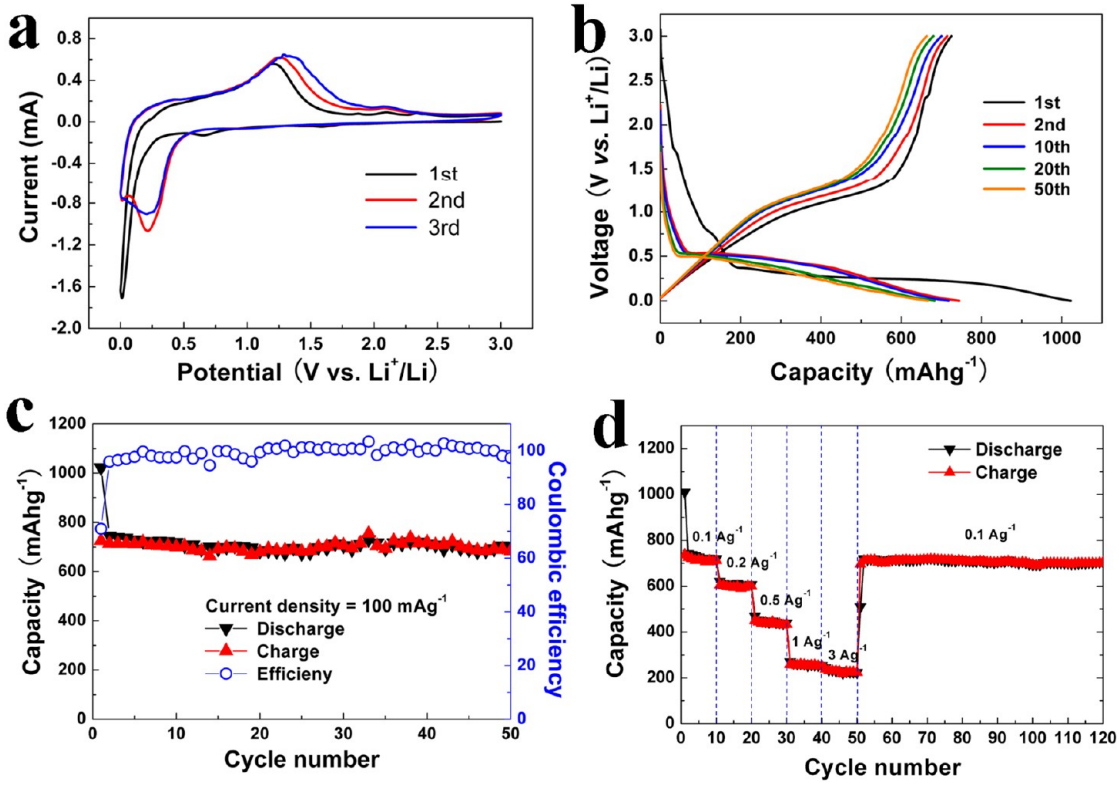

Figure 6. (a) CV curves at a scan rate of 0.1 mV s^{-1}. (b) Charge−discharge profiles of MnO/C electrodes at different cycles with a current density of 0.1 A g^{-1}. (c) Cycling performance and Coulombic efficiency at a 0.1 A g^{-1} current density. (d) Rate performances of MnO/C electrodes.

size distribution calculated from adsorption branches demonstrates the presence of bimodal porosity: 11 nm mesopores (2−50 nm) may be derived from the interleaved carbon matrix, and 87 nm macropores (>50 nm) might be arising from the interspace voids of the carbon matrix. These results are consistent with the STEM result in Figure 5b. Such porous structure can facilitate good contact of the internal active materials with electrolyte, leading to a fast transportation of Li^+ ions.[10,11] Meanwhile, the high specific surface area and porosity also are able to favorably alleviate the volume variation during the Li^+ insertion/extraction, resulting in a relatively high reversible capacity and excellent cycling performance.[14−17]

The electrochemical performance of MnO/C microspheres was evaluated by assembling CR2025 coin-type cells. The specific capacity is calculated by deducting the carbon content in this work. In Figure 6a, one pair of distinct redox peaks can be clearly identified from the cyclic voltammogram (CV) curves. The sharp reduction peak close to 0.1 V in the first cathodic sweep agrees well with the reduction of Mn^{2+} to Mn^0 and the formation of solid electrolyte interface (SEI) layers.[7] Then, it shifts to 0.3 V from the second cycle onward, suggesting an irreversible phase transformation due to the formation of Li_2O and metallic manganese.[4,5,11] A wide oxidation peak around 1.3 V appears in the anodic sweep, which can be attributed to the oxidation of Mn^0 to Mn^{2+}.[7,8] The profiles of CV curves in the subsequent cycles are overlapped well, demonstrating the good reversibility of the electrochemical reaction.

The charge−discharge profiles of the MnO/C sample at a current density of 0.1 A g^{-1} between 0.05 and 3 V are displayed in Figure 6b. Two distinct long voltage plateaus at around 0.5 and 1.2 V can be observed clearly during the discharge/charge process, matching well with the above CV analysis. The first discharge and charge capacities of the MnO/C sample are 1021.9 and 755.6 mAh g^{-1}, respectively. The large capacity loss in the first cycle is mainly attributed to the irreversible processes such as electrolyte decomposition and inevitable formation of the SEI layer.[3−7,9] However, from the second cycle onward, the MnO/C electrode shows the fascinating cycling stability (Figure 6c). The Coulombic efficiency steadily reaches around 99% accompanied by the cycle number increasing. At the end of the 50th cycle, a reversible capacity as high as 702.2 mAh g^{-1} can still be retained. Moreover, when the current density is increased from 0.1 to 3 A g^{-1}, the discharge and charge capacities remain stable and decrease regularly with an enhanced rate (Figure 6d). The corresponding reversible capacities at 0.1, 0.2, 0.5, 1, and 3 A g^{-1} are 741.8, 611.4, 452.6, 262.4, and 234.7 mAh g^{-1}, respectively. It is noticed that the capacities at higher currents faded rapidly, and the separations between the discharge plateaus and charge

plateaus were enlarged gradually in Figure S4. However, a satisfactory reversible capacity of 705 mAh g^{-1} still could be restored after another 60 cycles upon reducing the rate to 0.1 A g^{-1}. This phenomenon is mainly due to the kinetic-limited effects of the electrochemical conversion reaction in nature, rendering a higher overpotential and a lower capacity at a higher current. To further compare the electrochemical performance of various MnO-based anodes, we summarized the detailed information in Table S2. Apparently, in comparison to the previous literature,[3−20] our sample exhibits the remarkable specific capacity, the outstanding cycling stability, and excellent rate performance, which can be attributed to its unique hollow porous structure.

The direct evidence of the structural stability of the MnO/C electrode was revealed by TEM. Figure 7a clearly exhibits the TEM image of the MnO/C electrode

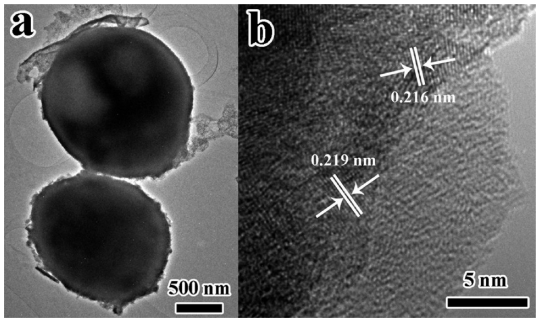

Figure 7. (a,b) TEM and HRTEM images of MnO/C microspheres charged to 3 V after 50 cycles at a 0.1 A g^{-1} current density.

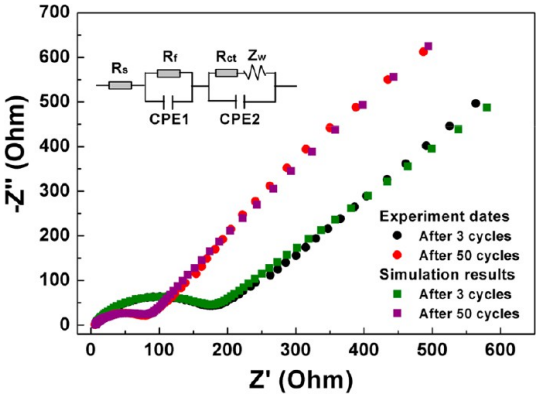

Figure 8. Nyquist plots and corresponding simulation results of MnO/C electrodes at 3.0 V (*vs* Li^+/Li). The inset is the equivalent circuit for plot fitting.

charged to 3 V after 50 charge/discharge cycles. These hollow porous MnO/C microspheres could maintain their original morphology. From the HRTEM image (Figure 7b), there is an amorphous layer on the surface of the MnO/C sample, which can be identified as the stable SEI layer. Meanwhile, lots of crystalline domains are well anchored in the carbon matrix. The fringe spacing values of these domains are about 0.22 nm, corresponding to (200) planes of MnO. No pulverization or size variation can be found in the MnO/C microspheres after repeated cycling, indicating that the hollow porous structure and carbon matrix can effectively accommodate the strain and stress of volume change and prevent the detachment and agglomeration of MnO during charge/discharge processes, which consequently enhances the cyclic stability and rate capability.

Figure 8 shows the Nyquist plots of the MnO/C electrode after 3 and 50 cycles. The electrochemical impedance spectroscopy (EIS) can be explained on the basis of an equivalent circuit model, as indicated in Figure 8. The intercept of the high-frequency semicircle on the Z' axis can be attributed to the resistance of electrolyte (R_s). The high-frequency semicircle corresponds to the SEI layer resistance (R_f) and capacitance (CPE1). The middle-frequency semicircle is associated with the charge transfer resistance (R_{ct}) and the double-layer capacitance (CPE2). The slope line at low frequency is related to the Warburg impedance (Z_w) of the lithium-ion diffusion. Generally, the large changes in R_f mean that the SEI layer is subjected to significant microstructural changes caused by the aggregation and pulverization of active materials upon repeated cycling.[19] In this work, a slight change in R_f implies that the MnO/C electrode has a stabilized SEI layer, as shown in Table 1. In addition, the obvious decrease of R_{ct} upon cycling would be ascribed to the hollow porous structure and the carbon matrix in the MnO/C electrode. The decreased R_{ct} allows better contact between the active material and electrolyte, achieves a high reaction area, and reduces the charge transfer resistance.[62]

SUMMARY AND CONCLUSIONS

In summary, we have successfully demonstrated a green and facile biotemplating method to fabricate MnO/C microspheres. The live *N. oculata* cells used in this work played multiple roles, which acted as

TABLE 1. Kinetic Parameters of N. oculata-Templated MnO/C Electrode

			CPE1			CPE2	
sample	R_s (Ω/cm^2)	R_f (Ω/cm^2)	Y	n	R_{ct} (Ω/cm^2)	Y	n
after 3 cycles	5.9	45.6	6.3×10^{-5}	0.58	128.5	7.6×10^{-4}	0.70
after 50 cycles	4.5	44.6	2.2×10^{-5}	0.67	51.4	8.1×10^{-4}	0.73

low-cost biotemplates to adsorb and take up metal ions *via* biosorption and acted as sustainable carbon sources to construct porous carbon matrices by the decomposition of carbonaceous organics. Owing to the unique hollow porous structure, MnO/C microspheres displayed superior electrochemical performances. The free volume in the hollow interior and the porosity in the shell could favorably accommodate the volume changes in electrochemical reactions and improve the accessibility of MnO hosts to lithium ions. The porous carbon matrix not only is effective in enhancing the electrical connectivity between MnO nanoparticles but also acts as an elastic barrier to buffer the stress of volume excursions and keep the structural integrity of MnO/C microspheres. The remarkable electrochemical performance suggests that this unique hierarchical hollow porous MnO/C could be a promising anode material for advanced lithium-ion batteries. We believe that this green, facile, and economical method will extend the scope of biotemplated synthesis to other materials for various applications such as catalysis, photonics, and gas sensing.

METHODS

Microalgae Culture. *Nannochloropsis oculata* cells (*N. oculata*) were originally obtained from Marine Biological Culture Collection Centre (China) and screened for its potential ability of growth at Zhejiang University of Technology (China). *N. oculata* cells were grown in the modified f/2 medium (a common and widely used general enriched seawater medium, for which the concentration of the original formulation, termed "f medium" (Guillard and Ryther 1962), has been reduced by half) in artificial seawater at room temperature (25 ± 1 °C) with a light intensity of 300 μmol m^{-2} s^{-1}. The *N. oculata* cells were collected after 15 days. The composition of artificial seawater (per liter) is as follows: 0.225 g of $NaNO_3$, 0.045 g of $NaH_2PO_4 \cdot H_2O$, 0.02 g of $Na_2SiO_3 \cdot 9H_2O$, 3.16 mg of $FeCl_3 \cdot 6H_2O$, 0.18 mg of $MnCl_2 \cdot 4H_2O$, 0.023 mg of $ZnSO_4 \cdot 7H_2O$, 4.36 mg of $Na_2 \cdot$EDTA, 0.01 mg of $CuSO_4 \cdot 5H_2O$, 0.012 mg of $CoCl_2 \cdot 6H_2O$, 0.07 mg of $Na_2MoO_4 \cdot 2H_2O$, 1 μg of vitamin B_1, 1 μg of vitamin B_{12}, and 0.5 μg of biotin.

Synthesis of Hollow Porous MnO/C Microspheres. First, *N. oculata* cells were concentrated and washed three times in deionized water to remove the unwanted materials. Then, 3.951 g of $KMnO_4$ (0.025 mol) and 3.551 g of Na_2SO_4 (0.025 mol) were dissolved into 100 mL of deionized water and formed a precursor solution for the coating process. Subsequently, 150 mL of concentrated *N. oculata* cells solution was added into the above precursor solution and immersed for 1 h at room temperature. After being immersed, the dark brown precipitates were filtered and washed and dried at 60 °C for 12 h in air. In order to obtain MnO/C microspheres, 0.2 g of the as-prepared precursor sample was placed inside an alumina boat, and 2 mL of 20 wt % of polystyrene (PS) suspended in dimethylformamide (DMF) was dropped onto the as-prepared precursor sample. Finally, the sample was calcined in a tube furnace at 500 °C for 4 h under a flowing nitrogen atmosphere.

Material Characterization. The phase purity and crystalline structure of the sample were collected using powder XRD (X'Pert Pro diffractometer, Cu Kα, λ = 1.5418 Å). X-ray photoelectron spectroscopy (XPS) analysis was conducted using an Al Kα (1486.6 eV) monochromatic X-ray source (Axis Ultra DLD, Kratos). The thermal analysis was determined by SDT Q600 (TA Instruments, U.S.A) under oxygen atmosphere at a heating rate of 10 °C min^{-1} from room temperature to 800 °C. Scanning electron microscopy (SEM, Hitachi S-4700) and transmission electron microscopy (TEM, FEI, Tecnai G^2 F30) equipped with an energy-dispersive spectroscopy (EDS) detector were used to investigate the microstructure of the sample and analyze its elements. The cross section scanning transmission electron microscopy (STEM) specimens were prepared by slicing the particles embedded in epoxy resin with a Reichert-Jung Ultracut E Ultramicrotome. The Raman spectrum was performed on a Renishaw InVia Raman spectrometer under a backscattering geometry (λ = 532 nm). Nitrogen adsorption−desorption was determined by Brunauer−Emmett−Teller (BET) tests using an ASAP 2020 (Micromeritics Instruments).

Electrochemical Measurements. The electrochemical performance of MnO/C microspheres was evaluated using CR2025 coin-type cells assembled in a glovebox under argon atmosphere. The working electrode was fabricated by mixing the active material (MnO/C), acetylene black, and polyvinylidene fluoride (PVDF) binder in the weight ratio of 7:2:1. The loading mass of each cathode is about 3 mg (2−3 mg cm^{-2}). The lithium foil was used as both counter electrode and reference electrode. A 1 M solution of $LiPF_6$ in ethylene carbonate and dimethyl carbonate (1:1 in volume) was used as the electrolyte with a Celgard membrane as the separator. The charge−discharge tests were performed on a Neware battery test system with galvanostatic in the voltage range of 0.05−3.0 V at room temperature. Cyclic voltammograms (CV) tests were performed by a CHI650B electrochemical workstation (Chenhua, Shanghai, China) in the voltage range of 0.05−3.0 V at a scan rate of 0.1 mV s^{-1}. Electrochemical impedance spectroscopy (EIS) measurements were tested with the frequency ranging from 0.1 to 10^6 Hz at room temperature by Zahner Zennium electrochemical workstation.

Conflict of Interest: The authors declare no competing financial interest.

Acknowledgment. The authors acknowledge financial support by the National Natural Science Foundation of China (51002138 and 51172205), the Natural Science Foundation of Zhejiang Province (LR13E020002 and LY13E020010), the Qianjiang Project of Zhejiang Province (2010R10029), the Scientific Research Foundation for the Returned Overseas Chinese Scholars (2010609), and New Century Excellent Talents in University (NCET 111079).

Supporting Information Available: Optical microscope image of *N. oculata*, TEM and HRTEM images of carbon residues derived from *N. oculata*, TEM-HRTEM-EDS analysis of the sample without PS coatings, EDS analysis of MnO/C microspheres, comparison of BET specific surface area and BJH pore size distribution of various MnO-based anode materials, discharge−charge curves of MnO/C electrodes at different current densities, and comparison of the electrochemical performances of various MnO anode materials. This material is available free of charge *via* the Internet at http://pubs.acs.org.

REFERENCES AND NOTES

1. Laruelle, S.; Grugeon, S.; Poizot, P.; Dolle, M.; Dupont, L.; Tarascon, J. M. On the Origin of the Extra Electrochemical Capacity Displayed by MO/Li Cells at Low Potential. *J. Electrochem. Soc.* **2002**, *149*, A627–A634.
2. Poizot, P.; Laruelle, S.; Grugeon, S.; Dupont, L.; Tarascon, J. M. Nano-Sized Transition-Metal Oxides as Negative-Electrode Materials for Lithium-Ion Batteries. *Nature* **2000**, *407*, 496–499.
3. Ding, Y. L.; Wu, C. Y.; Yu, H. M.; Xie, J.; Cao, G. S.; Zhu, T. J.; Zhao, X. B.; Zeng, Y. W. Coaxial MnO/C Nanotubes as Anodes for Lithium-Ion Batteries. *Electrochim. Acta* **2011**, *56*, 5844–5848.

4. Liu, Y. M.; Zhao, X. Y.; Li, F.; Xia, D. G. Facile Synthesis of MnO/C Anode Materials for Lithium-Ion Batteries. *Electrochim. Acta* **2011**, *56*, 6448–6452.
5. Li, X. W.; Li, D.; Qiao, L.; Wang, X. H.; Sun, X. L.; Wang, P.; He, D. Y. Interconnected Porous MnO Nanoflakes for High-Performance Lithium Ion Battery Anodes. *J. Mater. Chem.* **2012**, *22*, 9189–9194.
6. Zhong, K. F.; Zhang, B.; Luo, S. H.; Wen, W.; Li, H.; Huang, X. J.; Chen, L. Q. Investigation on Porous MnO Microsphere Anode for Lithium Ion Batteries. *J. Power Sources* **2011**, *196*, 6802–6808.
7. Sun, B.; Chen, Z. X.; Kim, H. S.; Ahn, H.; Wang, G. X. MnO/C Core−Shell Nanorods as High Capacity Anode Materials for Lithium-Ion Batteries. *J. Power Sources* **2011**, *196*, 3346–3349.
8. Liu, J.; Pan, Q. M. MnO/C Nanocomposites as High Capacity Anode Materials for Li-Ion Batteries. *Electrochem. Solid-State Lett.* **2010**, *13*, A139–A142.
9. Zhang, K. J.; Han, P. X.; Gu, L.; Zhang, L. X.; Liu, Z. H.; Kong, Q. S.; Zhang, C. J.; Dong, S. M.; Zhang, Z. Y.; Yao, J. H.; *et al.* Synthesis of Nitrogen-Doped MnO/Graphene Nanosheets Hybrid Material for Lithium Ion Batteries. *ACS Appl. Mater. Interfaces* **2012**, *4*, 658–664.
10. Xu, G. L.; Xu, Y. F.; Sun, H.; Fu, F.; Zheng, X. M.; Huang, L.; Li, J. T.; Yang, S. H.; Sun, S. G. Facile Synthesis of Porous MnO/C Nanotubes as a High Capacity Anode Material for Lithium Ion Batteries. *Chem. Commun.* **2012**, *48*, 8502–8504.
11. Li, X. N.; Zhu, Y. C.; Zhang, X.; Liang, J. W.; Qian, Y. T. MnO@1-D Carbon Composites from the Precursor $C_4H_4MnO_6$ and Their High-Performance in Lithium Batteries. *RSC Adv.* **2013**, *3*, 10001–10006.
12. Zhang, X.; Xing, Z.; Wang, L. L.; Zhu, Y. C.; Li, Q. W.; Liang, J. W.; Yu, Y.; Huang, T.; Tang, K. B.; Qian, Y. T.; *et al.* Synthesis of MnO@C Core−Shell Nanoplates with Controllable Shell Thickness and Their Electrochemical Performance for Lithium-Ion Batteries. *J. Mater. Chem.* **2012**, *22*, 17864–17869.
13. Hao, Q.; Xu, L. Q.; Li, G. D.; Ju, Z. C.; Sun, C. H.; Ma, H. Y.; Qian, Y. T. Synthesis of MnO/C Composites through a Solid State Reaction and Their Transformation into MnO_2 Nanorods. *J. Alloys Compd.* **2011**, *509*, 6217–6221.
14. Li, X. W.; Xiong, S. L.; Li, J. F.; Liang, X.; Wang, J. Z.; Bai, J.; Qian, Y. T. MnO@Carbon Core−Shell Nanowires as Stable High-Performance Anodes for Lithium-Ion Batteries. *Chem.—Eur. J.* **2013**, 10.1002/chem.201203553.
15. Sun, Y. M.; Hu, X. L.; Luo, W.; Huang, Y. H. Porous Carbon-Modified MnO Disks Prepared by a Microwave-Polyol Process and Their Superior Lithium-Ion Storage Properties. *J. Mater. Chem.* **2012**, *22*, 19190–19195.
16. Luo, W.; Hu, X. L.; Sun, Y. M.; Huang, Y. H. Controlled Synthesis of Mesoporous MnO/C Networks by Microwave Irradiation and Their Enhanced Lithium-Storage Properties. *ACS Appl. Mater. Interfaces* **2013**, *5*, 1997–2003.
17. Xu, G. L.; Xu, Y. F.; Fang, J. C.; Fu, F.; Sun, H.; Huang, L.; Yang, S. H.; Sun, S. G. Facile Synthesis of Hierarchical Micro/Nanostructured MnO Material and Its Excellent Lithium Storage Property and High Performance as Anode in a $MnO/LiNi_{0.5}Mn_{1.5}O_{4-\delta}$ Lithium Ion Battery. *ACS Appl. Mater. Interfaces* **2013**, *5*, 6316–6323.
18. Chen, W. M.; Qie, L.; Shen, Y.; Sun, Y. M.; Yuan, L. X.; Hu, X. L.; Zhang, W. X.; Huang, Y. H. Superior Lithium Storage Performance in Nanoscaled MnO Promoted by N-Doped Carbon Webs. *Nano Energy* **2013**, *2*, 412–418.
19. Liu, S. Y.; Xie, J.; Zheng, Y. X.; Cao, G. S.; Zhu, T. J.; Zhao, X. B. Nanocrystal Manganese Oxide (Mn_3O_4, MnO) Anchored on Graphite Nanosheet with Improved Electrochemical Li-Storage Properties. *Electrochim. Acta* **2012**, *66*, 271–278.
20. Mai, Y. J.; Zhang, D.; Qiao, Y. Q.; Gu, C. D.; Wang, X. L.; Tu, J. P. MnO/Reduced Graphene Oxide Sheet Hybrid as An Anode for Li-Ion Batteries with Enhanced Lithium Storage Performance. *J. Power Sources* **2012**, *216*, 201–207.
21. Chen, W. M.; Qie, L.; Shao, Q. G.; Yuan, L. X.; Zhang, W. X.; Huang, Y. H. Controllable Synthesis of Hollow Bipyramid β-MnO_2 and Its High Electrochemical Performance for Lithium Storage. *ACS Appl. Mater. Interfaces* **2012**, *4*, 3047–3053.
22. Fang, X. P.; Lu, X.; Guo, X. W.; Mao, Y.; Hu, Y. S.; Wang, J. Z.; Wang, Z. X.; Wu, F.; Liu, H. K.; Chen, L. Q. Electrode Reactions of Manganese Oxides for Secondary Lithium Batteries. *Electrochem. Commun.* **2010**, *12*, 1520–1523.
23. Guo, C. X.; Wang, M.; Chen, T.; Lou, X. W.; Li, C. M. A Hierarchically Nanostructured Composite of MnO_2/Conjugated Polymer/Graphene for High-Performance Lithium Ion Batteries. *Adv. Energy Mater.* **2011**, *1*, 736–741.
24. Yu, A. P.; Park, H. W.; Davies, A.; Higgins, D. C.; Chen, Z. W.; Xiao, X. C. Free-Standing Layer-By-Layer Hybrid Thin Film of Graphene-MnO_2 Nanotube as Anode for Lithium Ion Batteries. *J. Phys. Chem. Lett.* **2011**, *2*, 1855–1860.
25. Wang, H. Q.; Yang, G. F.; Li, Q. Y.; Zhong, X. X.; Wang, F. P.; Li, Z. S.; Li, Y. H. Porous Nano-MnO_2: Large Scale Synthesis *via* a Facile Quick-Redox Procedure and Application in a Supercapacitor. *New J. Chem.* **2011**, *35*, 469–475.
26. Xia, H.; Lai, M.; Lu, L. Nanoflaky MnO_2/Carbon Nanotube Nanocomposites as Anode Materials for Lithium-Ion Batteries. *J. Mater. Chem.* **2010**, *20*, 6896–6902.
27. Deng, Y. F.; Li, Z. N.; Shi, Z. C.; Xu, H.; Peng, F.; Chen, G. H. Porous Mn_2O_3 Microsphere as a Superior Anode Material for Lithium Ion Batteries. *RSC Adv.* **2012**, *2*, 4645–4647.
28. Qiu, Y. C.; Xu, G. L.; Yan, K. Y.; Sun, H.; Xiao, J. W.; Yang, S. H.; Sun, S. G.; Jin, L. M.; Deng, H. Morphology-Conserved Transformation: Synthesis of Hierarchical Mesoporous Nanostructures of Mn_2O_3 and the Nanostructural Effects on Li-Ion Insertion/Deinsertion Properties. *J. Mater. Chem.* **2011**, *21*, 6346–6353.
29. Wang, C. B.; Yin, L. W.; Xiang, D.; Qi, Y. X. Uniform Carbon Layer Coated Mn_3O_4 Nanorod Anodes with Improved Reversible Capacity and Cyclic Stability for Lithium Ion Batteries. *ACS Appl. Mater. Interfaces* **2012**, *4*, 1636–1642.
30. Li, L.; Guo, Z. P.; Du, A. J.; Liu, H. K. Rapid Microwave-Assisted Synthesis of Mn_3O_4-Graphene Nanocomposite and Its Lithium Storage Properties. *J. Mater. Chem.* **2012**, *22*, 3600–3605.
31. Gao, J.; Lowe, M. A.; Abruna, H. D. Spongelike Nanosized Mn_3O_4 as a High-Capacity Anode Material for Rechargeable Lithium Batteries. *Chem. Mater.* **2011**, *23*, 3223–3227.
32. Kim, S. W.; Han, T. H.; Kim, J.; Gwon, H.; Moon, H. S.; Kang, S. W.; Kim, S. O.; Kang, K. Fabrication and Electrochemical Characterization of TiO_2 Three-Dimensional Nanonetwork Based on Peptide Assembly. *ACS Nano* **2009**, *3*, 1085–1090.
33. Lou, X. W.; Archer, L. A.; Yang, Z. C. Hollow Micro-/Nanostructures: Synthesis and Applications. *Adv. Mater.* **2008**, *20*, 3987–4019.
34. Zhou, H.; Fan, T. X.; Zhang, D. Biotemplated Materials for Sustainable Energy and Environment: Current Status and Challenges. *ChemSusChem* **2011**, *4*, 1344–1387.
35. Shim, H. W.; Jin, Y. H.; Seo, S. D.; Lee, S. H.; Kim, D. W. Highly Reversible Lithium Storage in Bacillus Subtilis-Directed Porous Co_3O_4 Nanostructures. *ACS Nano* **2011**, *5*, 443–449.
36. Zhou, H.; Li, X. F.; Fan, T. X.; Osterloh, F. E.; Ding, J.; Sabio, E. M.; Zhang, D.; Guo, Q. X. Artificial Inorganic Leafs for Efficient Photochemical Hydrogen Production Inspired by Natural Photosynthesis. *Adv. Mater.* **2010**, *22*, 951–956.
37. Hall, S. R.; Swinerd, V. M.; Newby, F. N.; Collins, A. M.; Mann, S. Fabrication of Porous Titania (Brookite) Microparticles with Complex Morphology by Sol−Gel Replication of Pollen Grains. *Chem. Mater.* **2006**, *18*, 598–600.
38. Shim, H. W.; Lim, A. H.; Min, K. M.; Kim, D. W. Synthesis of Manganese Oxide Nanostructures Using Bacterial Soft Templates. *CrystEngComm* **2011**, *13*, 6747–6752.
39. Xia, Y.; Zhang, W. K.; Xiao, Z.; Huang, H.; Zeng, H. J.; Chen, X. R.; Chen, F.; Gan, Y. P.; Tao, X. Y. Biotemplated Fabrication of Hierarchically Porous NiO/C Composite from Lotus Pollen Grains for Lithium-Ion Batteries. *J. Mater. Chem.* **2012**, *22*, 9209–9215.
40. Pomerantseva, E.; Gerasopoulos, K.; Chen, X. Y.; Rubloff, G.; Ghodssi, R. Electrochemical Performance of the Nanostructured Biotemplated V_2O_5 Cathode for Lithium-Ion Batteries. *J. Power Sources* **2012**, *206*, 282–287.

41. Zhou, H.; Fan, T. X.; Zhang, D. Hydrothermal Synthesis of ZnO Hollow Spheres Using Spherobacterium as Biotemplates. *Microporous Mesoporous Mater.* **2007**, *100*, 322–327.
42. Tao, X. Y.; Du, J.; Li, Y. P.; Yang, Y. C.; Fan, Z.; Gan, Y. P.; Huang, H.; Zhang, W. K.; Dong, L. X.; Li, X. D. TaC Nanowire/Activated Carbon Microfiber Hybrid Structures from Bamboo Fibers. *Adv. Energy Mater.* **2011**, *1*, 534–539.
43. Shin, Y. S.; Wang, C. M.; Exarhos, G. L. Synthesis of SiC Ceramics by the Carbothermal Reduction of Mineralized Wood with Silica. *Adv. Mater.* **2005**, *17*, 73–77.
44. Tao, X. Y.; Dong, L. X.; Wang, X. N.; Zhang, W. K.; Nelson, B. J.; Li, X. D. B_4C-Nanowires/Carbon-Microfiber Hybrid Structures and Composites from Cotton T-Shirts. *Adv. Mater.* **2010**, *22*, 2055–2059.
45. Schnepp, Z.; Yang, W.; Antonietti, M.; Giordano, C. Biotemplating of Metal Carbide Microstructures: The Magnetic Leaf. *Angew. Chem., Int. Ed.* **2010**, *49*, 6564–6566.
46. Tao, X. Y.; Du, J.; Yang, Y. C.; Li, Y. P.; Xia, Y.; Gan, Y. P.; Huang, H.; Zhang, W. K.; Li, X. D. TiC Nanorods Derived from Cotton Fibers: Chloride-Assisted VLS Growth, Structure, and Mechanical Properties. *Cryst. Growth Des.* **2011**, *11*, 4422–4426.
47. Tao, X. Y.; Li, Y. P.; Du, J.; Xia, Y.; Yang, Y. C.; Huang, H.; Gan, Y. P.; Zhang, W. K.; Li, X. D. A Generic Bamboo-Based Carbothermal Method for Preparing Carbide (SiC, B_4C, TiC, TaC, NbC, $Ti_xNb_{1-x}C$, and $Ta_xNb_{1-x}C$) Nanowires. *J. Mater. Chem.* **2011**, *21*, 9095–9102.
48. Wu, X. L.; Wen, T.; Guo, H. L.; Yang, S. B.; Wang, X. K.; Xu, A. W. Biomass-Derived Sponge-like Carbonaceous Hydrogels and Aerogels for Supercapacitors. *ACS Nano* **2013**, *7*, 3589–3597.
49. Zhao, Y. F.; Wei, M.; Lu, J.; Wang, Z. L.; Duan, X. Biotemplated Hierarchical Nanostructure of Layered Double Hydroxides with Improved Photocatalysis Performance. *ACS Nano* **2009**, *3*, 4009–4016.
50. Kamata, K.; Suzuki, S.; Ohtsuka, M.; Nakagawa, M.; Iyoda, T.; Yamada, A. Fabrication of Left-Handed Metal Microcoil from Spiral Vessel of Vascular Plant. *Adv. Mater.* **2011**, *23*, 5509–5513.
51. Bigall, N. C.; Reitzig, M.; Naumann, W.; Simon, P.; van Pee, K. H.; Eychmuller, A. Fungal Templates for Noble-Metal Nanoparticles and Their Application in Catalysis. *Angew. Chem., Int. Ed.* **2008**, *47*, 7876–7879.
52. Guo, J. L.; Wang, X. L.; Liao, X. P.; Zhanga, W. H.; Shi, B. Skin Collagen Fiber-Biotemplated Synthesis of Size-Tunable Silver Nanoparticle-Embedded Hierarchical Intertextures with Lightweight and Highly Efficient Microwave Absorption Properties. *J. Phys. Chem. C* **2012**, *116*, 8188–8195.
53. Zahr, O. K.; Blum, A. S. Solution Phase Gold Nanorings on a Viral Protein Template. *Nano Lett.* **2012**, *12*, 629–633.
54. Li, X.; Chen, S. Y.; Hu, W. L.; Shi, S. K.; Shen, W.; Zhang, X.; Wang, H. P. *In Situ* Synthesis of CdS Nanoparticles on Bacterial Cellulose Nanofibers. *Carbohydr. Polym.* **2009**, *76*, 509–512.
55. Zhou, H.; Fan, T.; Zhang, D.; Guo, Q.; Ogawa, H. Novel Bacteria-Templated Sonochemical Route for the *In Situ* One-Step Synthesis of ZnS Hollow Nanostructures. *Chem. Mater.* **2007**, *19*, 2144–2146.
56. Zhou, H.; Fan, T. X.; Han, T.; Li, X. F.; Ding, J.; Zhang, D.; Guo, Q. X.; Ogawa, H. Bacteria-Based Controlled Assembly of Metal Chalcogenide Hollow Nanostructures with Enhanced Light-Harvesting and Photocatalytic Properties. *Nanotechnology* **2009**, *20*, 085603.
57. Nuraje, N.; Dang, X. N.; Qi, J. F.; Allen, M. A.; Lei, Y.; Belcher, A. M. Biotemplated Synthesis of Perovskite Nanomaterials for Solar Energy Conversion. *Adv. Mater.* **2012**, *24*, 2885–2889.
58. Bansal, V.; Poddar, P.; Ahmad, A.; Sastry, M. Room-Temperature Biosynthesis of Ferroelectric Barium Titanate Nanoparticles. *J. Am. Chem. Soc.* **2006**, *128*, 11958–11963.
59. Song, P.; Wang, Q.; Zhang, Z.; Yang, Z. X. Synthesis and Gas Sensing Properties of Biomorphic $LaFeO_3$ Hollow Fibers Templated from Cotton. *Sens. Actuators, B* **2010**, *147*, 248–254.
60. Cao, F.; Li, D. X. Biotemplate Synthesis of Monodispersed Iron Phosphate Hollow Microspheres. *Bioinspiration Biomimetics* **2010**, *5*, 16005.
61. Huang, M. J.; Wang, Y. J. Synthesis of Calcium Phosphate Microcapsules Using Yeast-Based Biotemplate. *J. Mater. Chem.* **2012**, *22*, 626–630.
62. Xia, Y.; Zhang, W. K.; Huang, H.; Gan, Y. P.; Xiao, Z.; Qian, L. C.; Tao, X. Y. Biotemplating of Phosphate Hierarchical Rechargeable $LiFePO_4$/C Spirulina Microstructures. *J. Mater. Chem.* **2011**, *21*, 6498–6501.
63. Lee, Y. J.; Yi, H.; Kim, W. J.; Kang, K.; Yun, D. S.; Strano, M. S.; Ceder, G.; Belcher, A. M. Fabricating Genetically Engineered High-Power Lithium-Ion Batteries Using Multiple Virus Genes. *Science* **2009**, *324*, 1051–1055.
64. Lam, M. K.; Lee, K. T. Microalgae Biofuels: A Critical Review of Issues, Problems and the Way Forward. *Biotechnol. Adv.* **2012**, *30*, 673–690.
65. Govindaraju, K.; Basha, S. K.; Kumar, V. G.; Singaravelu, G. Silver, Gold and Bimetallic Nanoparticles Production Using Single-Cell Protein (*Spirulina platensis*) Geitler. *J. Mater. Sci.* **2008**, *43*, 5115–5122.
66. Zaki, M. I.; Hasan, M. A.; Pasupulety, L.; Kumari, K. Thermochemistry of Manganese Oxides in Reactive Gas Atmospheres: Probing Redox Compositions in the Decomposition Course $MnO_2 \rightarrow MnO$. *Thermochim. Acta* **1997**, *303*, 171–181.